doi.org/10.26434/chemrxiv.11910873.v1

The Structures of Ordered Defects in Thiocyanate Analogues of Prussian Blue

Matthew Cliffe, Evan Keyzer, Andrew Bond, Maxwell A. Astle, Clare Grey

Submitted date: 28/02/2020 • Posted date: 02/03/2020

Citation information: Cliffe, Matthew; Keyzer, Evan; Bond, Andrew; Astle, Maxwell A.; Grey, Clare (2020): The Structures of Ordered Defects in Thiocyanate Analogues of Prussian Blue. ChemRxiv. Preprint. https://doi.org/10.26434/chemrxiv.11910873.v1

We report the structures of six new divalent transition metal hexathiocyanatobismuthate frameworks with the approximate formula MII[Bi(SCN)6]1−x · xH2O, M = Mn, Co, Ni and Zn. These frameworks are defective analogues of the perovskite-derived trivalent transition metal hexathiocyanatobismuthates MIII[Bi(SCN)6]. The defects in these new thiocyanate frameworks order and produce complex superstructures due to the low symmetry of the parent structure, in contrast to the related and more well-studied cyanide Prussian Blue analogues. Despite the close similarities in the chemistries of these four transition metal cations, we find that each framework contains a different mechanism for accommodating the lowered transition metal charge, making use of some combination of $Bi(SCN)_6^{3-}$ vacancies, M antisite defects, water substitution for thiocyanate, adventitious extra-framework cations and reduced metal coordination number. These materials provide an unusually clear view of defects in molecular framework materials and their variety suggests that similar richness may be waiting to be uncovered in other hybrid perovskite frameworks.

File list (4)

ARTICLE TYPE

Cite this: DOI: 10.1039/xxxxxxxxxx

The structures of ordered defects in thiocyanate analogues of Prussian Blue†

Matthew J. Cliffe,*[a,b] Evan N. Keyzer,[a] Andrew D. Bond,[a] Maxwell A. Astle[b] and Clare P. Grey[a]

We report the structures of six new divalent transition metal hexathiocyanatobismuthate frameworks with the approximate formula $M^{II}[Bi(SCN)_6]_{1-x} \cdot xH_2O$, M = Mn, Co, Ni and Zn. These frameworks are defective analogues of the perovskite-derived trivalent transition metal hexathiocyanatobismuthates $M^{III}[Bi(SCN)_6]$. The defects in these new thiocyanate frameworks order and produce complex superstructures due to the low symmetry of the parent structure, in contrast to the related and more well-studied cyanide Prussian Blue analogues. Despite the close similarities in the chemistries of these four transition metal cations, we find that each framework contains a different mechanism for accommodating the lowered transition metal charge, making use of some combination of $Bi(SCN)_6^{3-}$ vacancies, M_{Bi} antisite defects, water substitution for thiocyanate, adventitious extra-framework cations and reduced metal coordination number. These materials provide an unusually clear view of defects in molecular framework materials and their variety suggests that similar richness may be waiting to be uncovered in other hybrid perovskite frameworks.

1 Introduction

Defects are ubiquitous in functional materials and play a critical role in materials as simple as the binary rocksalt oxides[1,2] and as complex as high-temperature superconductors[3]. The importance of vacancy chemistry to molecular framework perovskites is becoming increasingly clear[4] in many important families, including the hybrid metal–halide semiconductors[5,6], cyanide Prussian Blue analogue battery cathodes[7,8] and magnetic formate perovskites[9,10], as the number of studies making use of defect-engineering in these materials grows. Perhaps the most widespread strategy for introducing defects is aliovalent doping, where an ion is replaced by an ion with a different charge. Thus far, cationic dopants have been the most widely used and have been introduced onto both the A, *e.g.* $NH_3CH_2CH_2NH_3^{2+}$ (EN^{2+}) substitutes for $CH_3NH_3^+$ (MA^+) in $CH_3NH_3[PbI_3]$ to produce 'hollow' perovskites,[5] and the B site, *e.g.* Fe^{2+} substitutes for Fe^{3+} in Prussian Blue[11]. In hybrid perovskites, these charged point defects are typically compensated by low-energy point defects of the opposite charge, most commonly vacancies, rather than by electronic defects.[12] For example, in the 'hollow' lead

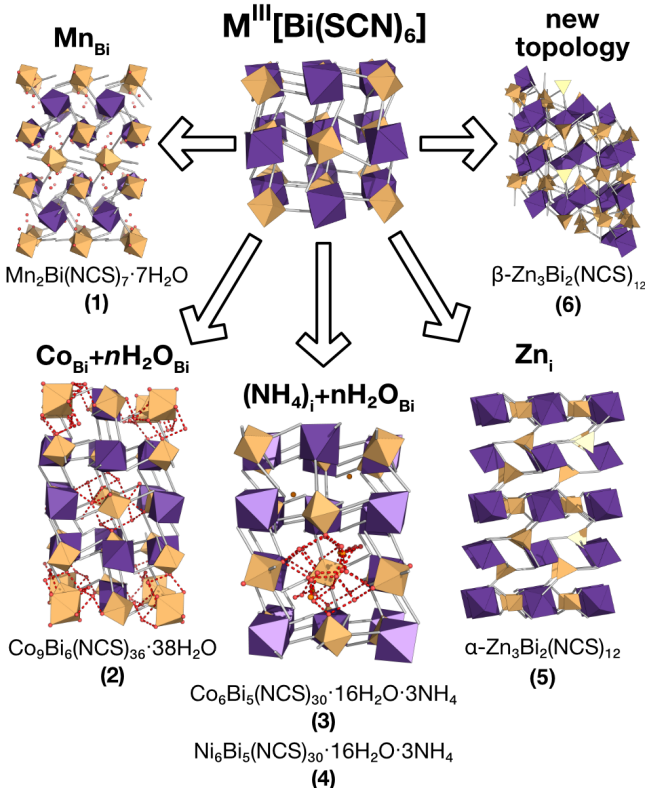

Fig. 1 Summary of the new defect-ordered thiocyanate Prussian Blue structures. Colour scheme: purple, Bi; orange, transition metal; NCS ligand, grey; and H_2O, NH_4 and hydrogen bonds, red.

[a] *Department of Chemistry, University of Cambridge, Lensfield Road, Cambridge CB2 1EW, UK;* [b] *School of Chemistry, University of Nottingham, University Park, Nottingham NG7 2RD, UK; E-mail: matthew.cliffe@nottingham.ac.uk*

† Electronic Supplementary Information (ESI) available, which includes details of synthesis, single crystal and powder X-ray diffraction and videos of symmetry-mode decomposition of structures. See DOI: 10.1039/b000000x/

‡ Additional footnotes to the title and authors can be included *e.g.* 'Present address:' or 'These authors contributed equally to this work' as above using the symbols: ‡, §, and ¶. Please place the appropriate symbol next to the author's name and include a `\footnotetext` entry in the the correct place in the list.

iodide perovskites, the additional A site charge is compensated primarily by vacancies on the B site, and can be represented in the Kröger-Vink defect notation by

$$2EN'_{MA} + V^{\cdot\cdot}_{Pb}. \quad (1)$$

However, this simplified defect reaction only provides a partial description of the structure of these defective materials. Bulk chemical analysis indicates that in addition to B site vacancies 'hollow' perovskites contain a substantial concentration of iodide vacancies, as much as 6%, and diffraction measurements indicate the presence of local defect-ordering beyond that visible in the average structure.[5] This example illustrates the general propensity for defective hybrid materials to contain both a wide diversity of point defects and for correlated defect disorder to emerge from the interactions between defects.

These two trends are just as important for the Prussian Blue analogue (PBA) family of cyanide frameworks. In Prussian Blue itself, the substitution of Fe^{2+} for Fe^{3+} is compensated by the formation of $Fe(CN)_6{}^{4-}$ vacancies:

$$4Fe(II)^{\cdot}_{Fe(III)} + V^{''''}_{Fe(III)(CN)6}, \quad (2)$$

leading to a final composition $Fe^{III}{}_4[Fe^{II}(CN)_6]_3 \cdot 14H_2O$.[11] A second composition, $M'^{II}{}_3[M^{III}(CN)_6]_2 \cdot xH_2O$, containing $M^{III}(CN)_6{}^{3-}$ vacancies also commonly occurs in PBAs.[13] These hexacyanometallate vacancies produce large voids which are filled with water clusters in the as-synthesised materials.[11,13] Both the vacancies and the water clusters play a critical role in determining the functional properties of these frameworks, including their mechanical robustness[14], their stability as pigments[15] and whether they show photomagnetism[16]. In addition, the ordering in space of these defects will likely play a key role in mass transport through these materials for applications including ionic conduction and gas sorption.[7,8,17,18]

PBAs also demonstrate one of the significant challenges of studying defective hybrid frameworks: it can be extremely difficult to determine their structures. Although dozens of compositions of PBAs have been reported,[17] they are typically produced as microcrystalline powders, which inherently limits the amount of information available through diffraction.[19] Even for single crystal and total scattering studies where information about the correlation of vacancies through the lattice can be obtained, the high symmetry of the parent structure means the local defect-structure determined through crystallography is superimposed on both the non-defective structure and the symmetry-related transformations of the defect, hindering detailed interpretation.[8,13,20,21] The presence of disorder also complicates the interpretation of spectroscopic data, as deconvolution of different defect sites can often be challenging unless there are additional helpful features such as moderate paramagnetism[22]. These problems are by no means unique to PBAs[9] and thus, despite the utility of accurate representations of defect-structures, we are often forced to resort to simplified models which omit the true complexity of defective molecular frameworks.

There is now growing interest in the potential of thiocyanate analogues of PBAs as functional materials,[23,24] and we have recently shown that hexathiocyanatobismuthate can be a versatile building block for the formation of Prussian Blue/perovskite-type structures $M[Bi(SCN)_6]$ (M = Sc^{3+}, Cr^{3+}, Fe^{3+}).[25] The thiocyanate anion imparts strong optical absorption to the framework through ligand to metal charge transfer bands and also introduces large octahedral tilts through the bent Bi–Ŝ–C bond angle, thereby significantly reducing both the symmetry and volume of the frameworks.

Table 1 Summary of reported compounds

	Formula	
1	$Mn_2Bi(SCN)_7 \cdot 7H_2O$	$V_{Bi(SCN)6}$; $[Mn(NCS)_2]_{Bi}$
2	$Co_9Bi_6(SCN)_{36} \cdot (H_2O)_{38}$	$V_{Bi(SCN)6}$; Co_{Bi}; $(H_2O)_n$
3	$Co_5Bi_6(SCN)_{30} \cdot 3NH_4 \cdot 16H_2O$	$V_{Bi(SCN)6}$; $(NH_4)_i$
4	$Ni_5Bi_6(SCN)_{30} \cdot 3NH_4 \cdot 16H_2O$	$V_{Bi(SCN)6}$; $(NH_4)_i$
5	α-$Zn_3Bi_2(SCN)_{12}$	Zn_i
6	β-$Zn_3Bi_2(SCN)_{12}$	new structure type

In this paper we investigate the defect chemistry of thiocyanate analogues of Prussian Blues by investigating the divalent analogues with the approximate composition $M_3[Bi(SCN)_6]$, M=Mn^{2+}, Co^{2+}, Ni^{2+} and Zn^{2+} [Table 1], in part inspired by previous partial reports of other transition metal thiocyanates hexthiocyanatobismuthates[26,27]. This aliovalent substitution introduces a high concentration of defects which, when combined with the low symmetry of the parent structure, produces long-range defect order. The presence of long-range order allows us to carry out detailed crystallographic investigations of both the identities and distribution of defects. We find that despite the close similarities between the chemistry of these transition metals, the defect structures are diverse, in both local structure and long-range order. We show that the point defects in these frameworks include $[Bi(SCN)_6]^{3-}$ vacancies, water clusters of up to 20 molecules, anti-site defects, and incorporation of interstitial charge-balancing cations. These point defects order into complex superlattice patterns which are, to the best of our knowledge, unknown in perovskites, both hybrid and conventional. We also find that where lower coordination-numbers are feasible for the transition metal, *e.g.* Zn^{2+}, new ordered structures can be favoured over defective frameworks. The range of chemistry found in these materials suggests that control over defects could produce surprising new chemical functionality throughout molecular perovskites.

2 Results and Discussion

2.1 Compound 1: $Mn_2Bi(SCN)_7$

Evaporation of a saturated solution of manganese carbonate in concentrated aqueous $H_3[Bi(SCN)_6]$ yields diffraction–quality single crystals of $Mn_2[Bi(SCN)_6](NCS) \cdot 7H_2O$, **1**, (synthetic details are available in the ESI†). Single crystal structure determination revealed that **1** is a defective thiocyanate Prussian Blue, where the aliovalent substitution of Mn(II) for every M(III) is compensated for by the introduction of one $Bi(SCN)_6{}^{3-}$ vacancy on one third of the Bi(III) sites [Fig. 2(a)]. These $Bi(SCN)_6{}^{3-}$

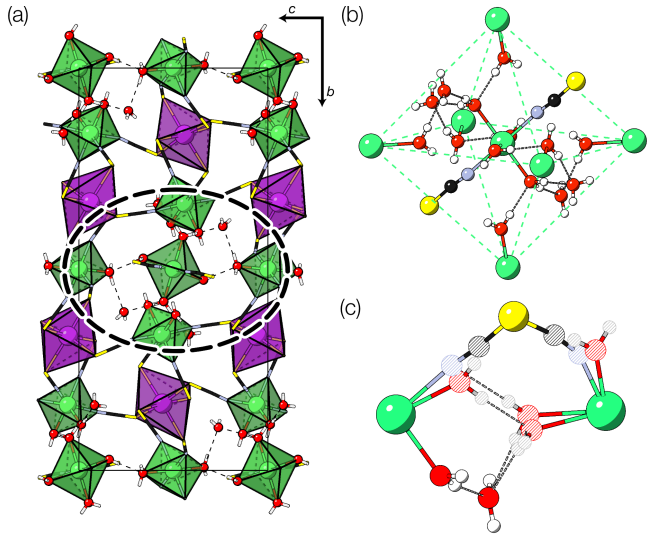

Fig. 2 (a) Crystal structure of $Mn_2[Bi(SCN)]_6(NCS)\cdot 7H_2O$ (**1**) at 300K. A dashed ellipse highlights the manganese molecular complex, shown in greater detail in (b). Disorder around the molecular cluster has been omitted in both (a) and (b) to aid visualisation. (c) A close-up view of the occupational disorder of the NCS and H_2O ligands in the vicinity of the molecular cluster. Colour scheme: purple, Bi; green, Mn; N, blue; C, black; S, yellow; red, O and white, H. Dashed lines indicate H-bonds, and partially occupied sites are indicated by striped circles.

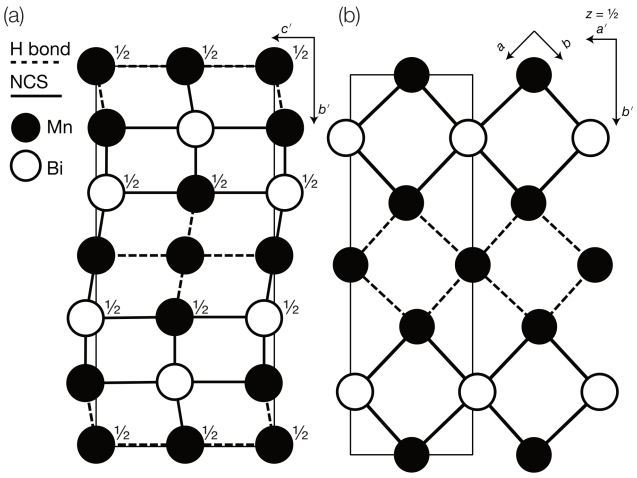

Fig. 3 Defect ordering pattern for **1**. (a) A view along the a axis. (b) A slice through the ab-plane, with $z \approx \frac{1}{2}$

vacancies are occupied by molecular aqua-Mn(II) thiocyanate complexes with average composition $Mn(H_2O)_5(NCS)^+$, connected to the framework by hydrogen bonds [Fig. 2(b)]. The positive charge on the molecular complex is balanced by an additional terminal framework thiocyanate which replaces a bound water. The formula can therefore also be written as $Mn[Bi(SCN)_6]_{1\text{-}x}\cdot x NCS\cdot x[Mn(H_2O)_5(NCS)]\cdot 9x(H_2O)$, $x=\frac{1}{3}$. The molecular Mn(II) complex is disordered and the charge-balancing thiocyanate are disordered, with the site bound to the framework occupied by water and thiocyanate in a 0.53:0.47 ratio, and the site bonded to the molecular Mn(II) complex showing the reverse. When the temperature of the crystal was raised to 300 K this ratio was found to be instead 0.7:0.3, indicating that a higher proportion of the NCS ligands are now bound to the framework, which suggests that there may be dynamic effects. The presence of disorder means that it was not possible to determine the relative proportions the $Mn(H_2O)_5(NCS)^+$ $Mn(H_2O)_6{}^{2+}$ or $Mn(H_2O)_4(NCS)_2$ complexes. [Fig. 2(c)].

The $Bi(SCN)_6{}^{3-}$ vacancies are long-range ordered and lie within every third (010) layer of metal atoms, corresponding to a {110}-type layer in the primitive cubic BX_3 aristotype. Within these (010) planes, all the $Bi(SCN)_6{}^{3-}$ are missing, so the structure comprises two successive non-defective layers followed by a third defective layer containing only Mn metal ions [Fig. 3]. This defect ordering pattern lowers the symmetry of the cubic aristotype to the orthorhombic *Immm* space group. When combined with the cooperative octahedral tilts produced by the bent M-SCN bonding, the structure lowers to the observed $P2_1/n$ space group. We confirmed that the observed framework structure is related to the parent structure within the descent-of-symmetry framework by using the ISODISTORT software package and Topas Academic [ESI Video 1].[†, 28–30] The resulting cell can be related to the $Pm\bar{3}m$ aristotype cell by the following transformation

$$\begin{pmatrix}\mathbf{a}'\\ \mathbf{b}'\\ \mathbf{c}'\end{pmatrix}=\begin{pmatrix}1 & -1 & 0\\ 3 & 3 & 0\\ 0 & 0 & 2\end{pmatrix}\begin{pmatrix}\mathbf{a}\\ \mathbf{b}\\ \mathbf{c}\end{pmatrix}, \qquad (3)$$

and is a $1\times 3\times 1$ supercell of the parent $M[Bi(SCN)_6]$ structure.

2.2 Compound 2: $Co_3Bi_2(NCS)_{12}$

Using an analogous route to the synthesis of **1** but substituting basic cobalt carbonate for manganese carbonate, we were able to synthesise a new framework of composition $Co_9Bi_6(NCS)_{36}(H_2O)_{38}$ (**2**). Compound **2** also has a defective Prussian Blue structure with missing hexathiocyanatobismuthate anions, however the mechanism by which this is accommodated is quite distinct from that of **1**. In **2** $Bi(SCN)_6$ vacancies order into alternate (001) layers, within which half of all $Bi(SCN)_6$ polyhedra are absent in a chequerboard fashion. This gives a total vacancy concentration of $\frac{1}{2}\times\frac{1}{2}=\frac{1}{4}$ [Fig. 4c].

The vacant sites are then filled by large 18 molecule water clusters in one half of the (001) layers and in the other half by charge balancing hydrated metal cations, $Co(H_2O)_6{}^{2+}\cdot 14H_2O$ cations [Fig. 4(a,b)]. The chemical formula can be therefore be alternatively written as $Co[Bi(SCN)_6]_{1\text{-}x}\cdot\frac{x}{2}Co(H_2O)_6(H_2O)_{14}\cdot\frac{x}{2}(H_2O)_{18}$, $x=\frac{1}{4}$.

Significant disorder is present for both the $(H_2O)_{18}$ and $Co(H_2O)_6{}^{2+}\cdot 14H_2O$ clusters, which prevents the determination of the hydrogen atom positions due to the large atomic displacement parameters. The complexity of the network means that the exact hydrogen bonding pattern remains unknown, though it is clear from the distances between O atoms and their geometric arrangement that significant hydrogen bonding is present. Six waters in each cluster coordinate to the framework Co(II) atoms, completing the octahedral coordination environment of the metal atoms. Comparison of the bond-valence sums of each of the Co atoms with literature values confirms that all framework transi-

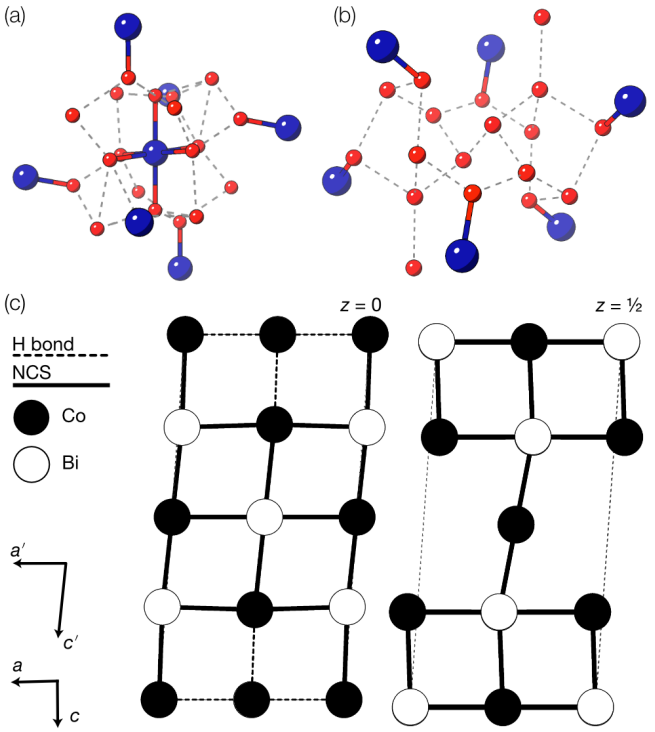

Fig. 4 Water clusters present in **2**: (a) $Co^{II}(H_2O)_6 \cdot 14H_2O$ and (b) $18H_2O$. Colour scheme: blue, Co and red, O. Dashed lines indicate H-bonds. (c) Ordering pattern for **2**, slice with $z = 0$ and $z = \frac{1}{2}$.

tion metal atoms remain in the Co(II) oxidation state. The hexaaquacobalt complex which occupies half the Bi vacancy sites has very enlarged atomic displacement parameters and significantly lengthened Co-O bond lengths compared to similar complexes. Elemental analysis (energy-dispersive X-ray spectroscopy on crystalline samples and ICP-OES on the framework dissolved in HNO_3) confirmed the absence of other adventitious cations such as Ca^{2+} and refinement of the structure with hexaquabismuth(III) produced a significantly worse quality of fit to the experimental diffraction data. As the refined structure show no other defects and in the absence of other plausible candidates, we therefore believe this cation is likely to be Co(II).

The observed defect ordering would, on its own, reduce the symmetry of the primitive cubic aristotype to a $2 \times 2 \times 4$ $I4/mmm$ structure, and when combined with octahedral tilting, this yields the resultant $2 \times 2 \times 4$ $P\bar{1}$ symmetry [ESI Video 2].† This structure relates to the M[Bi(SCN)$_6$] structure through the following transformation matrix:

$$\begin{pmatrix} \mathbf{a}' \\ \mathbf{b}' \\ \mathbf{c}' \end{pmatrix} = \begin{pmatrix} 1 & -1 & 0 \\ 1 & 1 & 0 \\ 0 & 0 & 2 \end{pmatrix} \begin{pmatrix} \mathbf{a} \\ \mathbf{b} \\ \mathbf{c} \end{pmatrix}. \quad (4)$$

2.3 Compounds 3 and 4: $M_6Bi_5(SCN)_{30} \cdot 3NH_4$, M = Co & Ni

We also explored the synthesis of frameworks using NH_4SCN. We found that by using NH_4SCN as a source of SCN^- and reacting it with $Co(NO_3)_2$ and $Bi(NO_3)_3$ using dilute HNO_3 as a solvent, small, diffraction quality single crystals of a new phase, $Co_6Bi_5(SCN)_{30} \cdot 16H_2O \cdot 3NH_4$ (**3**), formed rapidly, which incorporates NH_4 cations. Whereas our attempts to synthesise Ni-based frameworks using HSCN and basic Ni salts failed, we were able to use this new route to produce a new framework isostructural to **3**, $Ni_6Bi_5(SCN)_{30} \cdot 16H_2O \cdot 3NH_4$ (**4**). Single crystal diffraction revealed that **3** and **4** are defective perovskite frameworks containing $Bi(SCN)_6^{3-}$ vacancies, the structures of which can be thought of, like **2**, as {100} perovskite blocks separated by vacancy containing layers. Just as in **2**, these $Bi(SCN)_6^{3-}$ vacancies order in a chequerboard fashion in (100) layers, however, only every third layer contains vacancies and so the total vacancy concentration is $\frac{1}{6}$. The formula can therefore be alternatively written as $Co[Bi(SCN)_6]_{1-x} \cdot x[16H_2O \cdot NH_4] \cdot 2x(NH_4)$, $x = \frac{1}{6}$.

These vacancies compensate for half the negative charge introduced by substituting M(II) for M(III). The remaining charge is compensated by interstitial ammonium cations, which occupy two different sites, the first between two non-defective layers, and the second as part of the large 18 atom water cluster. This water cluster, like that in **2**, shows significant disorder, in part because each cluster lies across a centre of symmetry but contains only one NH_4^+ cation. The presence of the NH_4^+ cation was inferred from charge balance constraints, and which of the electron density peaks was NH_4^+ was decided on the basis of two factors: as it is half-occupied it will be the source of the disorder and it will be a better hydrogen bond donor than other water atoms. As we were unable to locate the H-atoms, definitive assignment of which molecule is NH_4^+ was not possible. This water cluster also coordinates to the Co sites which would be otherwise undercoordinated due to the $Bi(SCN)_6^{3-}$ vacancies.

The ordering of the Bi vacancies on the primitive lattice lowers the symmetry to *Cmmm* producing a $6 \times 2 \times 2$ supercell compared to $Pm\bar{3}m$, which then is lowered by the octahedral tilting, which has Glazer notation $c^-b^+a^-$ [ESI Video 3]†, to a triclinic cell related to the $Pm\bar{3}m$ by the following transformative matrix:

$$\begin{pmatrix} \mathbf{a}' \\ \mathbf{b}' \\ \mathbf{c}' \end{pmatrix} = \begin{pmatrix} 2 & 0 & 0 \\ 0 & 2 & 0 \\ -1 & 0 & 3 \end{pmatrix} \begin{pmatrix} \mathbf{a} \\ \mathbf{b} \\ \mathbf{c} \end{pmatrix}, \quad (5)$$

and to the M[Bi(SCN)$_6$] structure by

$$\begin{pmatrix} \mathbf{a}' \\ \mathbf{b}' \\ \mathbf{c}' \end{pmatrix} = \begin{pmatrix} 1 & 1 & 0 \\ -1 & 1 & 0 \\ -\frac{1}{2} & 0 & \frac{3}{2} \end{pmatrix} \begin{pmatrix} \mathbf{a} \\ \mathbf{b} \\ \mathbf{c} \end{pmatrix}. \quad (6)$$

2.4 Compounds 5 and 6: $Zn_3[Bi(SCN)_6]_2$

Addition of $Zn(NO_3)_2$ to a dilute HNO_3 solution of $H_3[Bi(SCN)_6]$ prepared from NH_4SCN produced single crystals over a period of minutes, and by single crystal X-ray diffraction we were able to solve two distinct polymorphic frameworks, α–$Zn_3[Bi(SCN)_6]_2$ (**5**) and β–$Zn_3[Bi(SCN)_6]_2$ (**6**) [Fig. 6]. Despite the similarity in synthesis route to that used for **3** and **4**, these new phases do not incorporate NH_4 from solution. In addition, unlike the other phases we describe, **5** and **6** do not contain lattice water and their

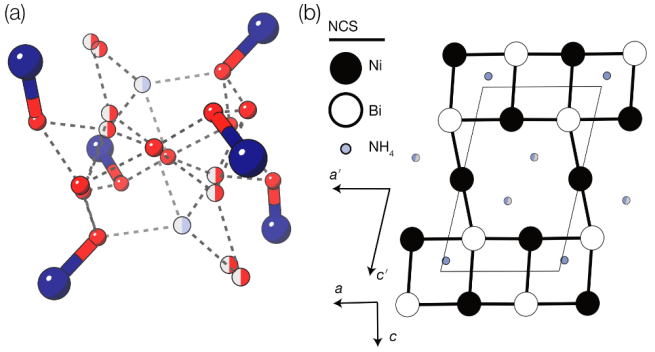

Fig. 5 (a) The $16(H_2O)\cdot NH_4$ cluster present in structure **3** (isostructural to that present in **4**). Colour scheme: dark blue, Co (Ni); red, O and light blue, N. Sites with half occupancy (e.g. O, N) are shown as split, half grey circles and dashed lines indicate H-bonds. Hydrogen atoms on the bound waters could not be located in the single crystal electron density maps and are not shown. (b) Ordering pattern for **3** and 4, slice with $z = 0$. Half occupied N sites are shown as half filled blue circles.

structures are much less closely related to that of $Fe[Bi(SCN)_6]$. Rietveld refinement of a polycrystalline sample confirmed that the polymorphs crystallise concomitantly, with the predominant fraction consisting of the β phase (92%) [ESI Fig. 1].† Careful examination of the powder X-ray diffraction data showed that the product contains at least one additional phase which we have been unable to isolate. As with the Prussian-Blue derived frameworks, the bent NCS–Bi bond angle leads to the formation of low symmetry structures, with multiple symmetry distinct metal sites in each (in α, two Bi and two Zn sites, and in β two Bi and three Zn sites).

The local connectivity is identical between the two phases, and there are only minor differences in bond lengths and angles. Despite these similarities, the topologies of framework connectivity of the α and β phases are very different. Indeed, by using the ToposPro software, we were able to determine that the graphs produced by considering the Zn_3Bi_2 sublattice for both $\alpha-$ and $\beta-Zn_3[Bi(SCN)_6]_2$ possess topologies which were not yet recorded in the ToposPro topology database.[31] We have termed these new topologies **clw1**, point symbol: $\{4^3.6^3\}2\{4^4.6^1 0.8\}\{4^4.6^2\}\{4^6.6^6.8^3\}$ and **clw2**, point symbol: $\{4^2.6^4\}\{4^3.6^3\}\{4^4.6^{11}\}\{4^4.6^2\}\{4^5.6^9.8\}$.

The α phase is derived from the parent phase by the incorporation of Zn^{2+} interstitials in half of all layers. More completely, it is built from two different layers, a Prussian Blue-like layer and CdI_2-like layer, which stack in an alternating fashion along the a axis to form a three-dimensional framework [Fig. 6(d)]. The Prussian Blue-like layer has the composition $ZnBi(SCN)_2$ and can be described as a {100} layer of a hypothetical '$ZnBi(NCS)_6$' analogue of the $Fe[Bi(NCS)_6]$ structure [Fig. 6(e)]. As the Zn is four-coordinated, its bonding requirements are saturated within the layer, and so the layer is connected to the layers above and below through the Bi atom. The second layer has composition $Zn_2Bi(NCS)_6\cdot NCS$ and a pseudo-CdI_2 structure, where the Bi ('Cd') atoms approximately form a triangular lattice, in which the interstices are occupied by Zn ('I') atoms [Fig. 6(f)]. In this layer, the Bi atoms are saturated by bonds within the layer, and so the

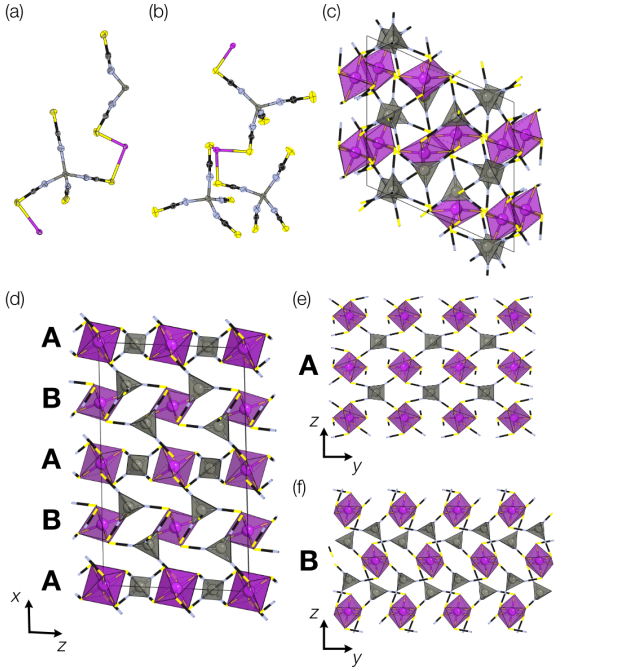

Fig. 6 Structures of α- and β $Zn_3Bi_2(SCN)_6$. Colour scheme: purple, Bi; grey, Zn; yellow, sulfur; blue, nitrogen and black, carbon. (a) Asymmetric unit of α-$Zn_3Bi_2(SCN)_6$, (b) asymmetric unit of β-$Zn_3Bi_2(SCN)_6$. (c) Unit cell of β-$Zn_3Bi_2(SCN)_6$, with coordination polyhedra drawn for the BiS_6 and ZnN_4. (d) Unit cell of α-$Zn_3Bi_2(SCN)_6$, viewed along the b direction, highlighting the alternating sequence of bc-layers along the a direction. The two kinds of layers are shown along b-direction showing (e) the pseudo-perovskite **A** and (f) pseudo-CdI_2 **B**.

connection to the other layer occurs through the Zn atoms, which are bound to an additional thiocyanate

The predominant size of ring in the β-$Zn_3Bi_2(NCS)_{12}$ phase is the sixteen-membered $Zn_2Bi_2(NCS)_4$ ring (four-membered ring, considering only metal cations) common to the $M[Bi(SCN)_6]$ perovskite. The ring–statistics are otherwise very different [Fig. 6(c)] and the structure cannot be easily decomposed into simple crystal-chemical units. The coordination geometry for both α and β phases remain similar, and there is only slightly larger variation in the octahedral coordination of BiS_6 distortions in the β phase.

The differences observed between Zn-based frameworks and the other transition metals derives from the increased favourability of the tetrahedral coordination, which permits the formation of charge-neutral and coordinatively saturated frameworks from $Zn(NCS)_4$ tetrahedra and $Bi(SCN)_6$ octahedra without the need for point vacancies or coordinating water molecules. This is directly akin to the cyanide Prussian Blue family, for which $Zn_3[Fe(CN)_6]_2$ can form both an ordered phase in which zinc is tetrahedrally coordinated, and a defective disordered cubic phase, analogous to the other Prussian Blues, in which Zn is octahedrally coordinated.[32] In $Zn_3[Fe(CN)_6]_2$, the polymorphism occurs between a disordered and an ordered phase, whereas both polymorphs of $Zn_3[Bi(SCN)_6]_2$ are ordered.

3 Discussion

To the best of our knowledge, the only previous reports of any compounds belonging to this family were by Cygański,[26,27] but in these early studies the analysis was confined principally to determining their composition. The following compositions were reported: $MnBi(SCN)_5$, $Mn_3[Bi(SCN)_6]_2 \cdot 7H_2O$, $Mn_3[Bi(SCN)_6]_2 \cdot 12H_2O$, $Ni_3[Bi(SCN)_6]_2 \cdot 10H_2O$, which do not correspond to any of the phases uncovered in our study; $Co_3[Bi(SCN)_6]_2 \cdot 12H_2O$ which corresponds approximately to **2**, and $Zn_3[Bi(SCN)_6]$ which corresponds to **5** and **6**. The fact that these early studies report compositions we have not yet synthesised ourselves indicates that perhaps there is even more latent complexity in this family of materials than we have uncovered.

Aside from **6**, all structures retain strong similarities to the parent $Fe[Bi(SCN)_6]$ structure, despite the stark differences in composition. If one normalises the cell volume by the number of Bi atoms, this normalised volume is within a few percent of $Fe[Bi(SCN)_6]$ for every compound, with the biggest discrepancy (5.5%) found for compound **6**. This suggests that the high vacancy concentration does not produce significantly contracted frameworks, which is likely due to the fact that potential voids are filled by water clusters and molecular complexes. For the compounds containing octahedrally coordinated transition metal ions, **1**-**4**, the pattern of tilts observed in the parent structure is retained [ESI Videos 1–3].† In addition, the (large) magnitude of the octahedral tilting is not significantly perturbed, as the primary source of tilts is the shape of the frontier orbitals of NCS^- and the resultant bent Bi-S-C bond angle. The retention of tilt-cooperativity in each of **1–4** is more surprising and is probably due in part to the presence of three dimensional connectivity of octahedra combined with the fact that no framework node has lower than four-fold coordination. These factors suggest that this $Fe[Bi(SCN)_6]$ structure type is robust and likely to be found in other members of this family, and is suggestive that porous analogues may well be possible.

The introduction of a divalent metal such as Mn^{2+} onto a trivalent metal site, M, introduces a single net negative charge, in the Kröger-Vink notation, $Mn_M^{'}$. As the framework is an overall charge-neutral insulator the framework must compensate by introducing charge balancing defects, and we found that there are a wide variety of mechanisms. α-$Zn_3[Bi(SCN)_6]$ can be thought of as containing Zn^{2+} interstitials:

$$2Zn_M^{\circ} + Zn_i^{\cdot\cdot}, \tag{7}$$

For the other transition metals, the transition metals retain octahedral coordination, even though tetrahedral Co(II) is well-known, and so they adopt structures more closely related to the $M[Bi(SCN)_6]$ structure. Compounds **1–4** all contain $Bi(NCS)_6^{3-}$ vacancies, and a key difference in these structures is how the resultant voids are filled and the open structures are stabilised. This is also a feature of the cyanide Prussian blues, which contain significant quantities of zeolitic water.[33] These thiocyanate frameworks have more complex structures than reported for PBAs, although similar complexity may be present in cyanide compounds but be more difficult to detect due to their higher symmetries. Compound **1**, contains molecular $Mn(NCS)_2(H_2O)_4$ complexes in the $V_{Bi(SCN)6}$ sites which are hydrogen-bonded to the network, instead of water clusters, summarised as:

$$3Mn_M^{'} + [Mn(NCS)_2]_{Bi(SCN)6}^{\cdots}. \tag{8}$$

Compound **2**, like **1**, contains anti-site type transition metal cations, which occupy half the $V_{Bi(SCN)6}$ sites. However, these Co^{2+} cations are not coordinated to thiocyanates, and water clusters occupy the remaining half of $V_{Bi(SCN)6}$ sites, that is:

$$8Co_M^{'} + V_{Bi(SCN)6}^{\cdots} + Co_{Bi(SCN)6}^{\cdot\cdot\cdot\cdot\cdot}. \tag{9}$$

The presence of other interstitial cations, such as NH_4^+ in **3** and **4**, adds an additional avenue for complexity, just as found in the cyanide Prussian Blues. Both **3** and **4** compensate for the effective negative charge of the divalent cation by the formation of $V_{Bi(SCN)6}$, which are all filled with water clusters, and ammonium cations:

$$6Ni_M^{'} + V_{Bi(SCN)6}^{\cdots} + 3(NH_4)_i^{\cdot}. \tag{10}$$

The ability of the thiocyanate perovskite framework to accommodate monovalent A-site cations has been previously demonstrated for $CsCd(NCS)_3$ [34] and $(NH_4)_2CdNi(NCS)_6$ [24].

4 Conclusion

We have found six new framework compounds of the approximate formula $M^{II}[Bi(SCN)_6]_{1-\frac{1}{3}}$. The primary mechanism by which the charge of aliovalent M(II) cations is accommodated by the frameworks is through the introduction of $Bi(SCN)_6$ vacancies, analogous to the $M(CN)_6$ vacancies found in the Prussian Blue; however anti-site defects, large water clusters and even neutral molecular metal complexes are also accommodated. In addition to this, we find that the low symmetry of the structure enables long-range order of these defects: we find that vacancies tend to segregate into {100} or {110} type layers. The complexity of these structures is such that single-crystal X-ray diffraction data is necessary to uncover it.

Despite the relatively high concentration of vacancies, we also found that the octahedral tilt patterns of the pattern structures are retained in all the Prussian Blue-derived members of this family, showing their robust nature. Compounds **3** and **4** demonstrate that as in the Prussian Blues, the presence of other cations can have a powerful effect on the resultant structure, as their incorporation leads to drastically different ordering patterns.

In conclusion, we have shed light on the surprising complexity of aliovalent doping in this family of hybrid framework materials. We anticipate that as the investigation of hybrid frameworks advances, the range of defects we have uncovered in thiocyanate frameworks will be reflected in other anion chemistries. These novel defect types will have different energetic formation costs, and the complex orderings will perturb the cooperative properties, such as mechanical flexibility and magnetism. The adaptability of these structures further suggests that guests of significant complexity, including molecular complexes, could be included in these frameworks, whether directly in synthesis or post-synthetically through ion-exchange processes.

5 Conflicts of Interest

There are no conflicts of interest to declare.

6 Acknowledgments

M.J.C. acknowledges the support of the School of Chemistry, University of Nottingham for the award of a Hobday Fellowship and Sidney Sussex College, University of Cambridge for financial support. E.N.K. thanks NSERC of Canada for a PGSD. Use of the Advanced Photon Source at Argonne National Laboratory was supported by the U. S. Department of Energy, Office of Science, Office of Basic Energy Sciences, under Contract No. DE-AC02-06CH11357.

References

1 F. Koch and J. B. Cohen, *Acta Crystallogr.*, 1969, **B25**, 275–287.

2 P. J. Saines, M. G. Tucker, D. A. Keen, A. K. Cheetham and A. L. Goodwin, *Phys. Rev. B*, 2013, **88**, 134418.

3 T. M. McQueen, Q. Huang, V. Ksenofontov, C. Felser, Q. Xu, H. Zandbergen, Y. S. Hor, J. Allred, A. J. Williams, D. Qu, J. Checkelsky, N. P. Ong and R. J. Cava, *Physical Review B*, 2009, **79**, 014522.

4 T. D. Bennett, A. K. Cheetham, A. H. Fuchs and F.-X. Coudert, *Nature Chemistry*, 2016, **9**, 11–16.

5 I. Spanopoulos, W. Ke, C. C. Stoumpos, E. C. Schueller, O. Y. Kontsevoi, R. Seshadri and M. G. Kanatzidis, *Journal of the American Chemical Society*, 2018, **140**, 5728–5742.

6 Y.-K. Jung, J. Calbo, J.-S. Park, L. D. Whalley, S. Kim and A. Walsh, *Journal of Materials Chemistry A*, 2019.

7 X. Wu, J. J. Hong, W. Shin, L. Ma, T. Liu, X. Bi, Y. Yuan, Y. Qi, T. W. Surta, W. Huang, J. Neuefeind, T. Wu, P. A. Greaney, J. Lu and X. Ji, *Nature Energy*, 2019, **4**, 123.

8 A. Simonov, T. De Baerdemaeker, H. L. B. Boström, M. L. Ríos Gómez, H. J. Gray, D. Chernyshov, A. Bosak, H.-B. Bürgi and A. L. Goodwin, *Nature*, 2020, **578**, 256–260.

9 M. Mączka, A. Gągor, K. Hermanowicz, A. Sieradzki, L. Macalik and A. Pikul, *Journal of Solid State Chemistry*, 2016, **237**, 150–158.

10 H. L. B. Boström, J. Bruckmoser and A. L. Goodwin, *Journal of the American Chemical Society*, 2019, **141**, 17978–17982.

11 H. J. Buser, D. Schwarzenbach, W. Petter and A. Ludi, *Inorg. Chem.*, 1977, **16**, 2704–2710.

12 A. Walsh, D. O. Scanlon, S. Chen, X. G. Gong and S.-H. Wei, *Angewandte Chemie International Edition*, 2015, **54**, 1791–1794.

13 P. Franz, C. Ambrus, A. Hauser, D. Chernyshov, M. Hostettler, J. Hauser, L. Keller, K. Krämer, H. Stoeckli-Evans, P. Pattison, H. B. Bürgi and S. Decurtins, *J. Am. Chem. Soc.*, 2004, **126**, 16472–16477.

14 H. L. B. Boström, I. E. Collings, A. B. Cairns, C. Romao and A. L. Goodwin, *Dalton Transactions*, 2019, **48**, 1647–1655.

15 F. Grandjean, L. Samain and G. J. Long, *Dalton Transactions*, 2016, **45**, 18018–18044.

16 A. Bleuzen, C. Lomenech, V. Escax, F. Villain, F. Varret, C. Cartier dit Moulin and M. Verdaguer, *Journal of the American Chemical Society*, 2000, **122**, 6648–6652.

17 S. S. Kaye and J. R. Long, *Catalysis Today*, 2007, **120**, 311–316.

18 K. W. Chapman, P. D. Southon, C. L. Weeks and C. J. Kepert, *Chemical Communications*, 2005, **0**, 3322–3324.

19 H. L. B. Boström and R. I. Smith, *Chemical Communications*, 2019.

20 A. Kumar, S. M. Yusuf, L. Keller and J. V. Yakhmi, *Physical Review Letters*, 2008, **101**, 207206.

21 D. Chernyshov and A. Bosak, *Phase Transitions*, 2010, **83**, 115–122.

22 A. Flambard, F. H. Köhler and R. Lescouëzec, *Angewandte Chemie International Edition*, 2009, **48**, 1673–1676.

23 H. Tabe, M. Matsushima, R. Tanaka and Y. Yamada, *Dalton Transactions*, 2019.

24 K.-P. Xie, W.-J. Xu, C.-T. He, B. Huang, Z.-Y. Du, Y.-J. Su, W.-X. Zhang and X.-M. Chen, *CrystEngComm*, 2016, **18**, 4495–4498.

25 M. J. Cliffe, E. N. Keyzer, M. T. Dunstan, S. Ahmad, M. F. L. D. Volder, F. Deschler, A. J. Morris and C. P. Grey, *Chemical Science*, 2019, **10**, 793–801.

26 A. Cyganski, *Roczniki Chemii*, 1963, **37**, 1543–1545.

27 A. Cyganski, *Roczniki Chemii*, 1964, **38**, 1699.

28 H. T. Stokes, D. M. Hatch and B. J. Campbell, *ISOTROPY Software Suite*.

29 B. J. Campbell, H. T. Stokes, D. E. Tanner and D. M. Hatch, *J. Appl. Crystallogr.*, 2006, **39**, 607–614.

30 A. Coelho, *TOPAS - Academic: General Profile and Structure Analysis Software for Powder Diffraction Data., Version 4.1*, Brisbane, Australia, 2007.

31 V. A. Blatov, A. P. Shevchenko and D. M. Proserpio, *Crystal Growth & Design*, 2014, **14**, 3576–3586.

32 J. Rodríguez-Hernández, E. Reguera, E. Lima, J. Balmaseda, R. Martínez-García and H. Yee-Madeira, *Journal of Physics and Chemistry of Solids*, 2007, **68**, 1630–1642.

33 F. Herren, P. Fischer, A. Ludi and W. Haelg, *Inorganic Chemistry*, 1980, **19**, 956–959.

34 G. Thiele and D. Messer, *Z. Anorg. Allg. Chem.*, 1980, **464**, 255–267.

The structures of ordered defects in thiocyanate Prussian Blue analogues

Matthew J. Cliffe,[*a,b] Evan N. Keyzer,[a] Andrew D. Bond,[a] Maxwell A. Astle[b] and Clare P. Grey[a]

February 28, 2020

[a] Department of Chemistry, University of Cambridge, Lensfield Road, Cambridge CB2 1EW, UK;
[b] School of Chemistry, University of Nottingham, University Park, Nottingham NG7 2RD, UK;
*To whom correspondence should be addressed; e-mail: matthew.cliffe@nottingham.ac.uk.

Contents

List of Figures

List of Tables

1 Synthetic Procedures

The synthesis procedures were adapted from those reported in[S1].

1.1 Synthesis of HSCN

In a 250 mL round bottom flask, NH_4SCN (5g, 65.7 mmol) was dissolved in 5 mL H_2O and cooled to 0 °C in an ice bath. A H_2SO_4 solution (ca. 7 ml of H_2SO_4 in 12 ml H_2O) was then added dropwise to the cooled NH_4SCN solution. The reaction mixture was stirred for 30 mins before being warmed to room temperature. The aqueous mixture was subsequently extracted with diethyl ether (2×20 ml) and the organic phase was retrieved and its volume reduced by half using a stream of N_2.

1.2 Synthesis of $H_3[Bi(SCN)_6]$ solution

$Bi_2O_2(CO_3)$ (0.50 g, 0.98 mmol) was suspended in ca. 12 mL H_2O followed by the addition of the HSCN/ether solution. The resulting reaction mixture was stirred vigorously under a slight flow of N_2 until all ether had been removed and the solution had turned bright orange. Any remaining solids were filtered off and the orange solution was placed under a slight vacuum to remove any excess HSCN.

1.3 Synthesis of 1

1mL of the prepared $H_3[Bi(SCN)_6]$ was added to approximately 50 mg $MnCO_3$, and left to react overnight. Any excess solids were removed by gravity filtration. The dark red solution was then left to evaporate in a watch glass covered by petri-dish for a period of approximate two weeks until diffraction quality dark orange single crystals formed.

1.4 Synthesis of 2

1mL of the prepared $H_3[Bi(SCN)_6]$ was added to approximately 50 mg ($Co_5(CO_3)_2(OH)_6$) and left to react overnight. Any excess solids were removed by gravity filtration. The dark red solution was then left to evaporate in a watch glass covered by petri-dish for a period of approximate two weeks until diffraction quality dark orange single crystals formed.

1.5 Synthesis of 3 and 4

$Bi(NO_3)_3 \cdot 2.5\,H_2O$ (3 mmol, 1.46 g) was dissolved in 1.5 mL 3M HNO_3, and a solution of NH_4SCN (13.1 mmol, 1.00 g) dissolved in 2 mL of distilled water was added to it, producing a vivid orange solution. $Ni(NO_3)_2 \cdot 6\,H_2O$ (7 mmol, 2.036 g) was dissolved in 2 mL of water and then added to to bismuth thiocyanate solution, which on standing produced numerous small very dark orange single crystals of **4** over a period of 15 min. The same route can be used to produce **3**, substituting $Co(NO_3) \cdot 6\,H_2O$.

1.6 Synthesis of 5 and 6

$Bi(NO_3)_3 \cdot 2.5\,H_2O$ (3 mmol, 1.46 g) was dissolved in 1.5 mL 3M HNO_3, and a solution of NH_4SCN (13.1 mmol, 1.00 g) dissolved in 2 mL of distilled water was added to it, producing a vivid orange solution. $Zn(NO_3)_2 \cdot 6\,H_2O$ (7 mmol, 2.082 g) was dissolved in 2 mL of water and then added to to bismuth thiocyanate solution, which on standing produced an immediate precipitate of numerous orange single crystals of **5** and **6**.

2 Single Crystal X-ray Diffraction

Single crystals were selected and mounted using perfluorinated oil on a polymer-tipped micromount and cooled rapidly to measurement temperature 120 K or 180 K in a stream of cold N_2 using an Oxford Cryosystems open flow cryostat. To enable variable temperature measurements, the crystal used for structures **1** and **1a** was mounted using varnish on a pin.

Single-crystal X-ray diffraction data for **2**, **4**, **5** and **6** were collected using a Nonius KappaCCD diffractometer, using graphite monochromated Mo$K\alpha$ radiation (λ = 0.7107 Å). Data for **1** and **1a** were collected using a on a Bruker D8-Quest PHOTON-100 diffractometer equipped with an Incoatec IμS Cu microsource ($\lambda = 1.54056$Å). Data for **3** were collected using Single crystal X-ray diffraction data were collected on an Oxford Diffraction GV1000 (AtlasS2 CCD area detector, mirror-monochromated Cu-K_α radiation source ($\lambda = 1.54184$Å). Structure solution was carried out using SHELXT and refinement with SHELXL, within the OLEX2 graphical interface.[S2–4] For crystal **1**, hydrogen atoms were refined with constrained geometries and riding thermal parameters, however the disorder present in samples **2**–**4** meant that hydrogen atoms could not be located, aside from an NH_4 cation in **4**. Disordered sites in structures **1**, **2**, **3** and **4** were modelled at half occupancy.

ESI Table 1: Summary of key crystallographic parameters for all compounds

Compound	**1**	**1a**	**2**
Formula	$Mn_2Bi(SCN)_7\,7\,H_2O$	$Mn_2Bi(SCN)_7\,7\,H_2O$	$Co_9Bi_6(SCN)_{36}\,(H_2O)_{38}$
Molar mass	851.54	851.54	4535.47
Crystal System	Monoclinic	Monoclinic	Triclinic
Space Group	$P2_1/n$	$P2_1/n$	$P\overline{1}$
Crystal Colour	dark orange	dark orange	dark orange
Z	4	4	1
Radiation	Cu K_α	Cu K_α	Mo K_α
Temperature (K)	300	180	180
a (Å)	8.3698(3)	8.3065(2)	12.0209 (2)
b (Å)	26.0037(9)	25.8428(6)	12.1613 (2)
c (Å)	12.2466(4)	12.2664(3)	23.8319 (4)
α (Å)	90	90	94.200 (1)
β (Å)	91.208(2)	90.2360(10)	94.003 (1)
γ (Å)	90	90	91.452 (1)
V (Å^3)	2664.83(16)	2633.12(11)	3464.52 (10)
Measured reflections	30850	33300	21789
Independent reflections	4712	4657	13585
$R_{\rm int}$	0.1315	0.080	0.035
$R[F^2 > 2\sigma(F^2)]$	0.0553	0.038	0.059
S	1.013	1.03	1.13
CCDC number			

Compound	**3**	**4**	**5**	**6**
Formula	$Co_5Bi_6(SCN)_{30}\,3\,NH_4\cdot 16\,H_2O$	$Ni_5Bi_6(SCN)_{30}\,3\,NH_4\cdot 16\,H_2O$	α-$Zn_3Bi_2(SCN)_{12}$	β-$Zn_3Bi_2(SCN)_{12}$
Molar mass	3438.91	3512.13	1311.03	1311.03
Crystal System	Triclinic	Triclinic	Monoclinic	Monoclinic
Space Group	$P\overline{1}$	$P\overline{1}$	$C2/c$	$P2_1/c$
Crystal Colour	dark orange	dark orange	orange	orange
Z	1	1	4	4
Radiation	Cu K_α	Mo K_α	Mo K_α	Mo K_α
Temperature (K)	120	111	109	180
a (Å)	11.9106 (3)	11.8567 (2)	26.3104 (4)	17.7331 (6)
b (Å)	11.9382 (3)	11.8653 (2)	8.4587 (1)	13.6501 (4)
c (Å)	8.4250 (5)	18.3824 (4)	15.7403 (3)	16.4375 (4)
α (Å)	83.935 (2)	84.0731 (7)	90	90
β (Å)	76.504 (2)	76.7140 (7)	93.630	114.3971 (12)
γ (Å)	85.384 (2)	85.1942 (8)	90	90
V (Å^3)	2529.04 (12)	2498.60 (8)	3496.00 (9)	3623.55 (19)
Measured reflections	37154	20614	7507	12934
Independent reflections	9921	11356	3975	7822
$R_{\rm int}$	0.047	0.050	0.029	0.052
$R[F^2 > 2\sigma(F^2)]$	0.031	0.043	0.026	0.051
S	1.03	1.04	1.07	1.05
CCDC number				

Cu K_α, $\lambda = 1.54056$Å, Mo K_α, $\lambda = 0.71073$Å.

3 Powder X-ray Diffraction

A high-resolution synchrotron X-ray powder diffraction measurement on a ground powder of $Zn_3Bi_2(NCS)_{12}$ was carried out at beamline 11-BM at the Advanced Photon Source (APS) using a wavelength of 0.414537 Å. The sample was loaded into a 0.8 mm diameter Kapton capillary. Rietveld refinement of the data was carried out using Topas Academic 4.1.[S5?] Lattice parameters were allowed to refine freely along with isotropic displacement parameters for Bi atoms and terms accounting for crystallite size broadening and crystallographic strain. The presence of a minor tertiary phase was modelled using independently refining peaks, which we were unable to index as a separate phase.

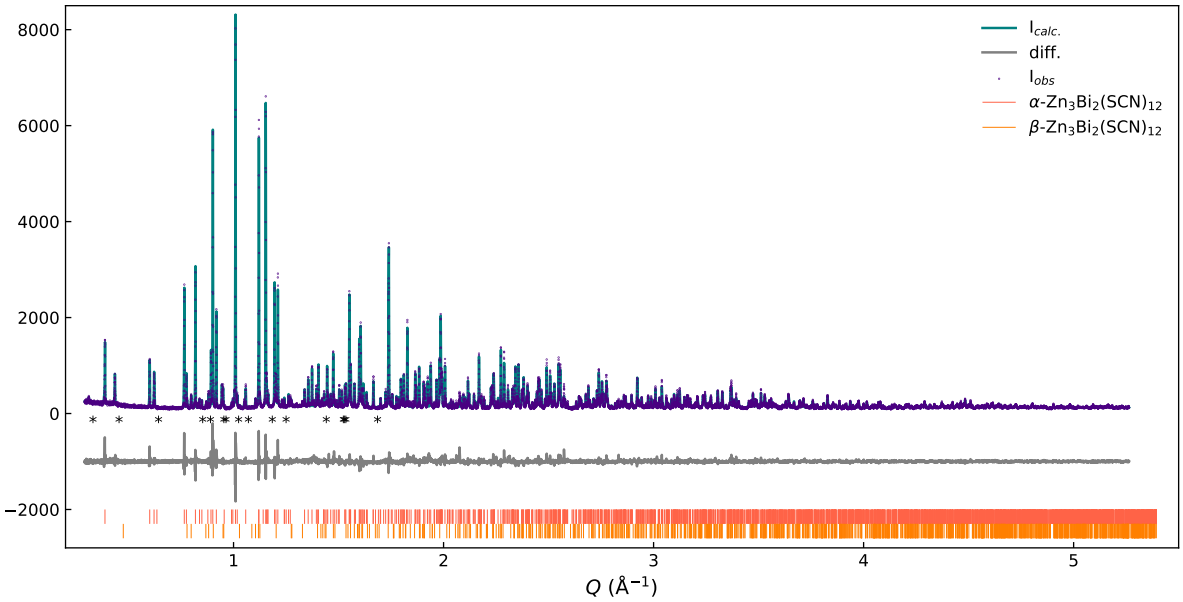

ESI Fig. 1: Rietveld refinement of mixed phase α- and β $Zn_3Bi_2(SCN)_6$. * indicates the presence of an impurity peak.

4 ICP-OES

Inductively coupled plasma optical emission spectroscopy (ICP-OES) was recorded on a Perkin Elmer, Optima 2000 DV ICP-OES with S10 autosampler. Samples and standards were prepared with a final solution composition of 2% nitric acid. Metal content was kept below 50 mg/L for ICP measurements as at higher concentrations a precipitate would form which would not dissolve in limited volumes of acids. Found for sample **2** Bi 27.35%, Co 17.97%, Ca 0.0%, Ni 0.0% and Ti 0.0%.

5 STEM-EDX

Energy dispersive X-ray (EDX) spectroscopy was acquired using dark field scanning transmission electron microscopy (STEM), performed using a JEOL JEM-2100+ microscope operated at 200 kV and an Oxford Instruments XMaxN 100TLE X-ray microanalysis system. Samples were deposited onto copper grid mounted "lacey" carbon films (Agar) and the beam was condensed to areas suspended over holes of the amorphous carbon to negate the contribution to the carbon signal from the support film. Copper contributions from the grid were discounted from the analysis. The measured proportions of light atoms (C, N and O) will have contributions from the carbon film and as these measurements were carried out under high vacuum, it is likely a significant proportion of lattice water will have been lost.

ESI Table 2: STEM-EDX elemental ratios in sample **2**

Element	Wt%	At%	At. Ratio	At. Ratio (calc.)
Bi	19.87	2.02	2	2
Co	9.74	3.51	3.47	3
S	20.14	13.32	13.19	12
C	23.9	42.18	41.76	12
N	21.61	32.71	33.39	12
O	4.72	6.25	6.19	12.67
Ca	0.02	0.01	0.01	0
Ti	0	0	0	0
Ni	0	0	0	0

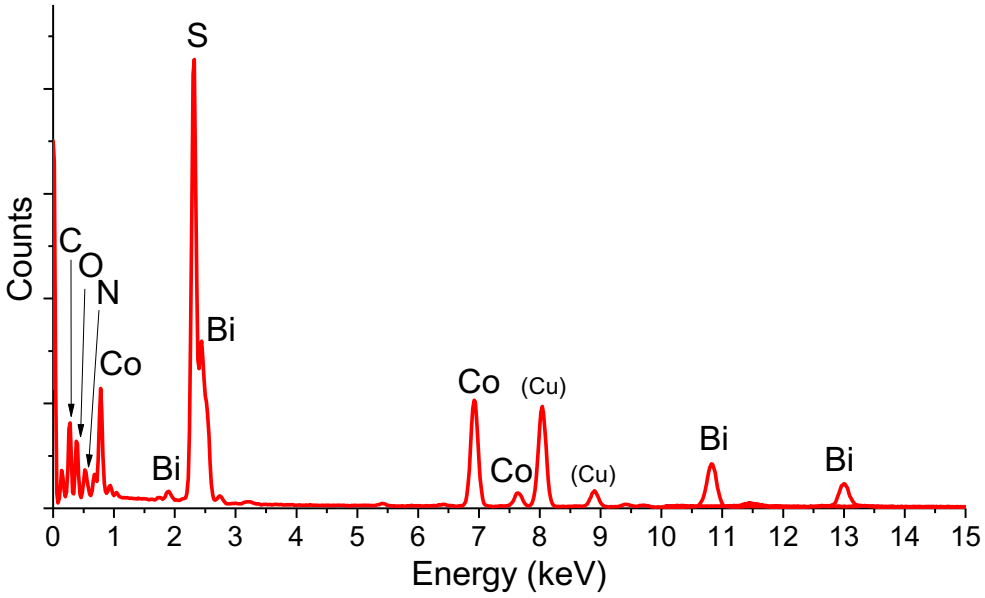

ESI Fig. 2: Representative EDX spectrum for compound **2**

References

(S1) M. J. Cliffe, *et al.*, *Chemical Science* **10**, 793 (2019).
(S2) O. V. Dolomanov, L. J. Bourhis, R. J. Gildea, J. A. K. Howard, H. Puschmann, *J. Appl. Crystallogr.* **42**, 339 (2009).
(S3) G. M. Sheldrick, *Acta Crystallogr.* **A71**, 3 (2015).
(S4) G. M. Sheldrick, *Acta Crystallogr.* **C71**, 3 (2015).
(S5) H. Rietveld, *J. Appl. Crystallogr.* **2**, 65 (1969).

Other files

videos.zip (4.22 MiB)	view on ChemRxiv • download file
structures_consolidated.zip (3.57 MiB)	view on ChemRxiv • download file